Reversible cation migration virtually eliminates voltage decay and hysteresis in lithium-rich layered oxides

*Donggun Eum[1, †], Byunghoon Kim[1, †], Sung Joo Kim[1], Hyeokjun Park[1], Jinpeng Wu[2,3], Sung-Pyo Cho[43], Gabin Yoon[1], Myeong Hwan Lee[1], Sung-Kyun Jung[1,5 4], Wanli Yang[3], Jinpeng Wu[5, 6], Won Mo Seong[1], Kyojin Ku[1], Wanli Yang[6], Orapa Tamwattana[1], Sung Kwan Park[1], Insang Hwang[1], and Kisuk Kang[1,6 2, 7 *]*

[1]Department of Materials Science and Engineering, Research Institute of Advanced Materials (RIAM), Seoul National University, 1 Gwanak-ro, Gwanak-gu, Seoul 151-742, Republic of Korea.

[2]Stanford Institute for Materials and Energy Sciences, SLAC National Accelerator Laboratory, Menlo Park, CA, USA.

[3]The Advanced Light Source, Lawrence Berkeley National Laboratory, Berkeley, CA, USA.

[4]National Center for Inter-University Research Facilities, Seoul National University, Seoul National University, 1 Gwanak-ro, Gwanak-gu, Seoul 151-742, Republic of Korea.

[5]Next Generation Battery Lab, Material Research Center, Samsung Advanced Institute of Technology (SAIT), Samsung Electronics Co., Ltd., 130 Samsung-ro, Yeongtong-gu, Suwon-si, Gyeonggi-do 16678, Republic of Korea.

⁶Center for Nanoparticle Research, Institute for Basic Science (IBS), Seoul National University, 1 Gwanak-ro, Gwanak-gu, Seoul 151-742, Republic of Korea.

⁷Institute of Engineering Research, College of Engineering, Seoul National University, 1 Gwanak-ro, Gwanak-gu, Seoul 151-742, Republic of Korea

†These authors contributed equally to this work.

*Corresponding author: Kisuk Kang

E-mail: matlgen1@snu.ac.kr

Abstract

Despite the high energy density of lithium-rich layered-oxide electrodes, their real-world implementation in batteries is hindered by the substantial voltage decay on cycling. This voltage decay is widely accepted to mainly originate from progressive structural rearrangements involving irreversible transition metal migration. As prevention of this spontaneous cation migration has proven difficult, a paradigm shift toward management of its reversibility is needed. Herein, we demonstrate that the reversibility of the cation migration of lithium-rich nickel manganese oxides can be remarkably improved by altering the oxygen stacking sequences in the layered structure and thereby dramatically reducing the voltage decay. The preeminent intra-cycle reversibility of the cation migration is experimentally visualized and first-principles calculations reveal that an O2-type structure restricts the movements of transition metals within the Li layer, which effectively streamlines the returning migration path of transition metals. Furthermore, we propose that the enhanced reversibility mitigates the asymmetry of the anionic redox in conventional lithium-rich electrodes, promoting the high-potential anionic reduction, thereby reducing the subsequent voltage hysteresis. Our findings demonstrate that regulating the reversibility of the cation migration is a practical strategy to reduce voltage decay and hysteresis in lithium-rich layered materials.

With the advent of electrified transportation, there is a pressing demand for improvements of rechargeable lithium-ion batteries.[1] In particular, the energy-density ceiling placed on the cathode materials has been a primary factor precluding the full-scale deployment of green energy technologies.[2] Among cathode materials foreseen to transcend such limitations, lithium-rich layered oxides hold the greatest promise because of their high reversible capacity (exceeding 250 mAh g^{-1}) and high-voltage anionic redox chemistry.[3,4] Nonetheless, the ~~inevitable~~ voltage decay, or gradual decrease in the average discharge voltage during cycling, and the resulting inevitable energy decay remain~~s one~~ some of the most pernicious problems jeopardizing their real-world application, while some technical hurdles such as lower crystallographic/tap densities than current lithium-stoichiometric layered oxides (lithium nickel-cobalt-aluminum oxides and lithium nickel-manganese-cobalt oxides) still need to be addressed.[4-6] Moreover, the voltage decay is pronounced in 3d metal-based layered lithium-rich oxides of practical interest, such as Li[Li$_x$Ni$_y$Mn$_{(1-x-y)}$]O$_2$ (denoted as LLNMOs) and Li[Li$_x$Ni$_y$Mn$_z$Co$_{1-x-y-z}$]O$_2$ (denoted as LLNMCOs).[4,7,8] With this backdrop, formidable research efforts have been focused on unraveling the origin of the voltage decay and suppressing it based on established understandings.

A clear consensus has been reached that the voltage decay is primarily rooted in progressive structural transformation of lithium-rich layered oxides.[6,7,9-11] Cation migration from the transition metal (TM) layer to the Li layer to form TM$_{Li}$–V$_{TM}$ anti-site defect pairs during the charging of lithium-

rich layered 3d metal oxides has been identified experimentally and confirmed using various analytical tools.[9,11,12] The limited reversibility of intra-cycle TM migration results in the cumulative formation of a spinel-like disordered phase[12-14], and this growth of the low-voltage spinel-like phase has commonly been associated with voltage decay. [14-16] More specifically, a comprehensive investigation of the $Li_2Ru_{1−x}M_xO_3$ (M = Mn, Ti, Sn) system[6] and LLNMCOs[11,17] demonstrated that upon extended cycling, more TM ions were trapped in the Li layer with exacerbated voltage fade. Of paramount importance in understanding the fundamentals of the voltage decay is that its essential determinant is not the TM migration itself but the resulting confinement of TM ions in the Li layer. At the low Li stoichiometries of most lithium-rich layered oxides, TM migration to the Li layer is thermodynamically favorable and is thus an ~~inseparable~~ ==unavoidable== phenomenon during the charge process.[18-20] Therefore, although various effective approaches, including surface coating,[12] cation doping,[21] additives to electrolyte,[22] and composition tuning,[7,23] have been used to mitigate the TM migration, its ultimate prevention during long-term cycling has not yet been achieved.

Considering both the underlying origin of the voltage decay and the inevitability of TM migration, a substantive key lies in improving the intra-cycle reversibility of TM migration. In lithium layered oxides, what limits the reversible return of TM ions is thought to be the intralayer movements of TM ions within the Li layer, which is generally initiated by the TM migration from the initial tetrahedral site to neighboring octahedral sites

in Li layer. For example, in conventional O3-type layered oxides, TM ions once migrated to the intermediary tetrahedral site of the Li layer can readily and permanently move to adjacent octahedral Li sites because of the thermodynamic preference for octahedral sites, as indicated by the yellow arrow in **Fig. 1**a.[24] Therefore, the quest for reversible TM migration necessitates the implementation of thermodynamic or kinetic roadblocks that prevent intralayer movements of TM ions. In terms of thermodynamic approaches, recent reports on sodium layered oxides have suggested that the use of distinct oxygen lattices with the P3-[25,26] or P2-[27] structure can prevent the TM occupation of guest-ion sites benefiting from the size mismatch between the TM ion and the large prismatic site. In a similar vein, a qualitative hypothesis has been proposed in studies on lithium layered oxides that by employing an O2-type layered structure with ABCBA oxygen stacking[28] (see **Fig. 1**b), some Li sites can be thermodynamically destabilized against TM migration.[29,30] The local environments of Li sites in the O2 and O3 structures substantially differ: LiO_6 octahedra share faces with TMO_6 octahedra in the former, whereas they share only edges with TMO_6 octahedra in the latter. Thus, in the O2 structure, TM migration from the intermediate sites to adjacent Li sites is expected to be unfavorable because of the large electrostatic repulsion between face-shared cations. This blockade of face-shared sites can facilitate the return of TM ions during the discharge process by streamlining the return path, as illustrated in **Fig. 1**b. However, despite these implications, no direct approach has been reported to observe or

6

achieve reversible TM migration by utilizing an alternative oxygen lattice for lithium-rich layered oxides.

In this work, we first demonstrate that reversible intra-cycle TM migration can be achieved by modifying the oxygen lattice of lithium-rich layered oxides. To achieve this aim, we apply the O2 structure to cobalt-free LLNMOs with archetypal TM composition to obtain the O2-phase $Li_x(Li_{0.2}Ni_{0.2}Mn_{0.6})O_2$ (x $\approx$ 0.83), whose preliminary electrochemical activity was very recently reported.[31] We demonstrate that O2-LLNMOs inherently allow reversible intra-cycle TM migration, thus delivering outstanding voltage retention over extended cycling and far outperforming their O3-phase counterparts and other lithium-rich layered 3d metal oxides. Structural characterization using scanning transmission electron microscopy (STEM), X-ray Diffraction (XRD), Raman spectroscopy, and high-resolution TEM (HR-TEM) analyses reveal that the suppressed voltage decay arises from the retention of the pristine layered structure with highly reversible TM migration over extended cycling. In addition, with the aid of first-principles calculations, it is shown that high energy penalties associated with the TM occupation of Li sites of O2-LLNMOs prevent movements of TM ions in Li layer, facilitating the return of TM ions to the original sites. We further confirm that the improved reversibility of TM migration also benefits mitigating the asymmetry of the anionic redox, which has been suspected to stem from the presence of TM ions in the Li layer during discharging and afflict the cells by inducing voltage hysteresis.[10,32,33] Our findings indicate that tailoring the migration path of

TM ions provides a viable strategy to address the issues of voltage decay and hysteresis, which may help rejuvenate the research field of lithium-rich layered oxides.

Electrochemistry of O2-LLNMOs

O2-LLNMOs were synthesized by applying ion-exchange method to as-synthesized P2-phase sodium layered oxides. Details on the crystal structure and chemical compositions, $Li_x(Li_{0.2}Ni_{0.2}Mn_{0.6})O_2$ (x ≈ 0.83), are provided in Supplementary Discussion 1. **Fig. 2**a presents the first and second charge–discharge curves of O2-LLNMOs cycled in the voltage range of 2.0–4.8 V at 5 mA g^{-1}. A capacity of 235 mA g^{-1} was delivered for the first charge process of the O2-LLNMOs. Unlike the first cycle of the O3-$Li(Li_{0.2}Ni_{0.2}Mn_{0.6})O_2$, which was synthesized for a more precise comparison, the O2-LLNMOs delivered a markedly reduced irreversible capacity of 13.5 mAh g^{-1}, in comparisons with the first irreversible capacity of 74.3 mAh g^{-1} for O3-type counterparts (Supplementary Fig. 3), implying highly reversible first-cycle redox behavior. Scanning transmission X-ray microscopy (STXM) analysis, which enables bulk-sensitive characterization of the redox centers[34,35], identified that the oxidation states of Ni and Mn in pristine O2-$Li_x(Li_{0.2}Ni_{0.2}Mn_{0.6})O_2$ were close to +2 and +4, respectively (Supplementary Fig. 4).[36,37] Upon initial charging, cationic Ni^{2+}/Ni^{4+} redox occurs in the low-voltage region, whereas the oxidation of the oxygen non-bonding states accounts for the charge compensation of the high-voltage

8

plateau region. Further in-depth characterization of the redox mechanism and meticulous comparison of the O2 and O3 phases will be elaborated later.

For the initial two cycles (**Fig. 2**a), it is notable that the voltage profile of the second discharge was almost identical to that of the first discharge except for a small decrease in the capacity. To further clarify the long-term voltage retention of the O2-LLNMOs, cycling for additional 40 cycles was performed. **Fig. 2**b presents the discharge profile of the O2-LLNMOs for the first and every 10 cycles until 40 cycles. Negligible voltage decay was observed in the discharge of the O2-LLNMOs during the 40 cycles. The average discharge voltages were well preserved and close to 3.5 V (see inset in **Fig. 2**b): 3.53, 3.53, and 3.48 V for the 1st, 20th, and 40th discharge process, respectively. This outstanding voltage retention and the high redox voltage of O2-LLNMOs are in stark contrast with that of the O3 phase, which revealed severe voltage fades in the same electrochemical cycling (Supplementary Fig. 5), in accordance with many previous reports.[7,12,14,38] Comparison of the dQ dV^{-1} profiles tells clear suppression of the voltage decay in the O2-LLNMOs compared with that in the O3-LLNMOs (**Fig. 2**c). In the low-voltage region, a drastic down-shift of voltage was observed for the O3-LLNMOs upon cycling, and the major electrochemical activity was observed near 3.0 V (*vs*. Li/Li$^+$) even after 10 cycles. In contrast, this change was absent and the redox peaks remained constant in the O2-LLNMOs, with the primary redox activity maintained between 3.5 and 4.0 V (*vs*. Li/Li$^+$). The cycle stability of the O2-LLNMOs in

Fig. 2d was comparable to that of the O3-LLNMOs, indicating that the retention of the practical energy density of the O2-LLNMOs <mark>($\approx$ 82.5 %, 599.6 Wh kg^{-1} after 40 cycles)</mark> was superior to that of the O3-LLNMOs <mark>($\approx$ 71.8 %, 550 Wh kg^{-1} after 40 cycles)</mark> because of the suppressed voltage decay.

Reversible cation migration in O2-LLNMOs

To understand the origin of the remarkable voltage retention of the O2-LLNMOs from the perspective of structural transitions, we carefully probed the configuration of the TM ions using spherical-aberration-corrected scanning transmission electron microscopy (Cs-STEM). **Fig. 3**a and b present high-angle annular dark-field (HAADF) images of samples in charged and discharged states, respectively. HAADF images were obtained using Z-contrast imaging, and thus, the predominant signals in the images belong to heavy transition metals.[27,39] In the HAADF-STEM image of the pristine O2-LLNMOs (Supplementary Fig. 6), alternating TM layers and Li layers are clearly visible with no signal of TM ions detected in the Li layer, confirming the absence of TM_{Li}–V_{TM} anti-site defects in the pristine state. In addition, the dumbbell-like spots in TM layers indicate the $Li^+Mn^{4+}_6$ or $(Li^+_xNi^{2+}_{1-x})Mn^{4+}_6$ honeycomb ordering in the pristine O2-LLNMOs, which is a typical signature of lithium-rich layered materials (Supplementary Discussion 2).[7,50] In contrast, the HAADF image for the charged samples ($\sim$4.8 V *vs*. Li/Li$^+$) provided in **Fig. 3**a reveals the noticeable presence of

TM ions in the Li layer. The signal profile along the vertical direction in the box in **Fig. 3**a shows the evolution of new peaks at the center of two adjacent TM layers, as denoted by the arrows. These peaks suggest that a substantial amount of TM ions occupy vacant Li sites during the charge process. Selected area electron diffraction (SAED) patterns along the $[1\bar{1}0]$ axis also confirm the same TM behavior over a much broader region (150× magnified), with new diffraction spots as highlighted in the yellow boxes in **Fig. 3**c. To assign these spots, we simulated SAED patterns assuming the disordered O2 structure in which 25% of TM ions occupy octahedral sites or tetrahedral sites in the Li layer (Supplementary Fig. 7). The consistency between the experimental and simulated patterns indicates that massive TM migration occurred during the charge process, which is consistent with the TM migration behavior observed for the charge process of O3-LLNMOs.[11,33] Surprisingly, in the STEM image of the fully discharged O2-LLNMOs, no signal of TM ions in the Li layer was detected (**Fig. 3**b). Contrast to the charged state, the peaks between the TM layers completely disappeared in the HAADF signal profile, indicating the complete return of TM ions to the TM layer upon discharge. The SAED pattern of the discharged samples no longer contained characteristic spots of TM_{Li} defects (the yellow boxes in **Fig. 3**c,) as observed in **Fig. 3**d. The STEM analyses unequivocally confirm that interlayer TM migration is highly reversible during the successive charge and discharge of O2-LLNMOs. This phenomenon has not been observed in other lithium-rich layered oxides that contain a considerable amount of 3d TMs such as Mn

11

and Ni.[11,33]

We performed first-principles calculations to elucidate the energetics of the TM migrations that enable this reversible behavior in O2-LLNMOs. **Fig. 3**e presents schematic illustrations of the interlayer migration paths of TM ions in the O2 and O3 structures, respectively (see Supplementary Discussion 3 for details). In the case of O3 structure, TM ions can migrate to the nearest neighboring tetrahedral site in the Li layer and subsequently to the octahedral Li site during the charge process. On the other hand, in the O2 structure, TM ions can either migrate to the neighboring tetrahedral intermediate site (path A) or octahedral intermediate site (path B), followed by subsequent migration to the final octahedral (path A) and tetrahedral sites (path B), respectively. For these potential migration paths for O3 and O2 structures, we comparatively calculated the relative site energies of the intermediate and final sites considering all the possible TM configurations. **Fig. 3**f presents the energy landscapes of selected cases in which migration to the intermediate site was the most thermodynamically feasible (see Supplementary Tables 3–5 for the energetics of other cases). When TM ions move in the O3 structure, the lowest relative site energy of the intermediate site is estimated to be −0.19 eV, and that of the adjacent Li octahedral site ("$Edge_{octa}$") is −0.06 eV. It indicates that once TM ion moves to the intermediate site, further migration to the adjacent octahedral Li site is quite feasible. It would inevitably complicate the return of the TM ions to the initial site. TM ions may be led astray by further interactions with Li ions or other TM ions in

12

the Li layer, making the return of TM ions to the original TM site nearly impossible. However, for TM ions in the O2 phase, the relative site energy at the final Li site is substantially higher (0.520.27 and 0.91 eV for path A ("Face$_{octa}$") and path B ("Face$_{tetra}$"), respectively) destabilizing TM occupancy, whereas the TM in intermediate sites may remain stable in the de-lithiated states. These results suggest that TM migrations to the Li layer occur in the charged states, as observed in **Fig. 3**a, but that further intra-layer migration in the Li layer is significantly inhibited in the O2 structure. The intra-layer migration along paths A and B in the O2 structure requires a thermodynamic penalty of approximately 0.660.91 and 1.19 eV, respectively. And, while these values are obtained for the cases in which a moving TM ion share a face with Mn in the TM layer, the site energies at face-sharing sites are all positive in the O2 structure, regardless of the type of cations that faces the moving TM ion (see Supplementary Discussion 3). This result is reasonable considering that the final Li sites in the O2 phase share a face with cations in the TM layer, as shown in **Fig. 1**b. Because TM ions in O2-LLNMOs are predicted to remain in the original or intermediate sites during charging, they can readily return to the original sites upon re-lithiation, as demonstrated in **Fig. 3**b.

To further verify the reversible cation migration in O2-LLNMOs over extended cycling, powder XRD analysis of the pristine and 10-, 20-, and 40-cycled electrodes was conducted (**Fig. 4**a and Supplementary Table 6). The XRD pattern of the pristine state contains well-defined honeycomb

13

superstructure peaks at 2θ = 20.8°, 24.2°, 29.1°, and 33.3°, which correspond to (1/3 1/3 0), (1/3 1/3 1), (1/3 1/3 2), and (1/3 1/3 3) planes, respectively.[30] Each superstructure peak is well preserved even after 40 cycles, which indicates that the honeycomb orderings in the discharged samples were not destroyed by any permanent TM migrations, further supporting the reversibility of TM migration upon extended cycling. This behavior contrasts with that of the O3 phase, which typically loses in-plane cation ordering in the TM layers as the amount of TM/Li disordering increases with prolonged cycling.[6,11,33]

 Raman spectroscopy analysis was also conducted to determine the changes in the bonding character during cycling. **Fig. 4**b presents Raman spectra of the pristine and cycled O2-LLNMOs in the 300–700 cm^{-1} range whose peaks are attributed to the various vibration modes of TM–O bonding in lithium layered oxides.[13,36] The first two peaks at 595 and 473 cm^{-1} are signatures of symmetric stretching (A_{1g}) and symmetrical deformation (E_g) of TM–O, respectively, in the layered structure, whereas the peak at 420 cm^{-1} arises from the $LiMn_6$ honeycomb ordering, which is exclusively observed in lithium-rich layered oxides. Notably, all of these Raman peaks were observed for both samples and were preserved even after 40 cycles. This finding clearly contrasts with the case for O3-LLNMOs. Previous studies have shown that the Raman peak at 595 cm^{-1} completely shifted to 572 cm^{-1} only after 5 cycles because of the substantial layered-to-spinel phase transformation of O3-LLNMOs.[13,36] According to these previous reports, the peak at 627 cm^{-1} can be attributed to the

symmetrical stretching of TM–O in the spinel domain, and the peak at 572 cm^{-1} results from the shift of the peak at 595 cm^{-1} in a new TM coordinating environment.[13] Although we also detected peaks at 627 and 572 cm^{-1} after 40 cycles, their intensities were much smaller than those in previous reports on O3-LLNMOs.[7,13] In principle, the spinel phase formation in the O2 phase is inaccessible via room-temperature electrochemical cycling because the oxygen lattices are essentially incompatible, and phase transition requires major breakage of the strong metal–oxygen bonds.[29,40] Therefore, the evolution of these new peaks is likely to originate from the O3 phase impurity present in the sample during the pre-ion-exchange step.

HR-TEM analysis also supports the long-term structure preservation of O2-LLNMOs. As observed in Supplementary Fig. 10 and **Fig. 4**c, the characteristic hexagonal $P6_3mc$ spot patterns were consistently observed both for the pristine and 40-cycled O2-LLNMOs. There were no signatures of any secondary phases, including a spinel-like phase or the traces of TM/Li disordering, in the patterns of the 40-cycled electrodes. More specifically, compared with the simulated pattern of the disordered O2 structure (Supplementary Fig. 11), characteristic spots such as $1\bar{1}0$, $0\bar{1}\bar{3}$, and $10\bar{3}$ pertaining to the disordered phase did not appear in the SAED pattern or its signal profile (**Fig. 4**c). This result differs from that for O3-LLNMOs, in which the spots of the spinel-like and disordered phase evolved only after 5 cycles.[7] The comparisons of structural evolution in the O2 and O3 phases using complementary XRD, Raman, and HR-TEM

analyses clearly demonstrate that the global and local structures of the O2-LLNMOs are well maintained over extended cycling, benefiting from the preeminent reversibility of TM migration unlike conventional LLNMOs, which lose the structural integrity in a few cycles.

High-potential O redox behavior preserved in O2-LLNMOs

Notably, recent studies on lithium-rich layered oxides have demonstrated the intrinsic coupling between the anionic redox and cation migration.[33,34] According to mechanistic investigation of LLNMCOs, TM migration to the Li layer decreases the redox potential of oxygen by >1 V, thereby leading to asymmetry of the anionic redox between charge and discharge.[33] This asymmetrical behavior of the anionic redox has been alleged to play a detrimental role in triggering voltage hysteresis, which exacerbates the voltage retention along with voltage decay phenomenon.[10,32,41,42] However, considering the reversibility of TM migration in O2-LLNMOs, a distinct anionic chemistry in contrast to the conventional mechanism is expected for O2-LLNMOs. To corroborate this hypothesis, we closely examined the evolution of redox couples during the charge and discharge of O2-LLNMOs. **Fig. 5**a shows the change in the O K-edge and Ni, Mn L$_3$-edge absorbance spectra determined from STXM analysis during the first cycle of O2-LLNMOs. The ~~five~~ six points in **Fig. 5**a correspond to the (1) pristine, (2) 4.5-V charged, (3) 4.8-V charged, (4)

3.8-V discharged, (~~4~~5) 3.4-V discharged, and (~~5~~6) 2.0-V discharged states, and the differences in the absorbance between two ~~consecutive~~ designated points are shown below. The results indicate that the charge process is compensated by the redox of Ni^{2+}/Ni^{4+} at relatively low voltage (3.3–4.5 V) and subsequently by O^{2-}/O^{n-} (n< 2) redox at high voltage (4.5–4.8 V), as previously discussed. When charging from 3.3 to 4.5 V ('1' → '2'), a peak appears at 856 eV in the Ni L_3-edge spectra with the simultaneous emergence of a low-energy peak around 529 eV in the O K-edge spectra, signifying the depopulation of the hybridized Ni_{3d}–O_{2p} antibonding state.[33,43] From 4.5 to 4.8 V ('2' → '3'), the peak at 531.~~5~~0 eV evolves in the O K-edge spectra, which is indicative of oxygen redox states at high potentials.[33] This oxygen redox is further evidenced by mapping of resonant inelastic X-ray scattering (mRIXS) analysis (**Fig. 5**b Supplementary Discussion 4). ~~Comparing with conventional X-ray photoelectron spectroscopy and X-ray absorption spectroscopy~~We note that, ~~the~~ O-K mRIXS has recently been demonstrated as a tool-of-choice for detecting the lattice oxygen redox states ~~a powerful capability on isolating the oxidized oxygen feature from the TM-O hybridization feature, thus has been regarded as the most reliable spectroscopic tool to fingerprint the oxygen redox~~ in both Li- and Na-ion battery electrodes.[33,34,44,45] In ~~mRIXS images~~particular, the emergence of a distinct feature at 531.0 eV excitation energy and 523.7 eV emission energy (red circles in **Fig. 5**b) indicates the presence of oxidized lattice oxygen~~s~~ in battery electrodes.[33] The results show that ~~While th~~such~~is~~ oxidized oxygen

17

~~redox~~ feature is absent in mRIXS ~~images of '1' and~~until '2', ~~but~~it becomes distinct in ~~the image of~~ '3', demonstrating oxygen oxidation at high potentials ('2' → '3') ~~again~~. No characteristic peaks are observed in the Mn L_3-edge STXM spectra throughout the entire charging regime, confirming the redox-inactive properties of Mn^{4+}. Ni and Mn K-edge X-ray absorption near edge spectroscopy (XANES) analyses (Supplementary Fig. ~~13~~12) also revealed a consistent redox mechanism during the charging process. Overall, the charging of O2-LLNMOs accompanies the sequence of redox couples, which is the same as that for their O3-type counterparts.[36,37] This accordance is reasonable considering that the tendency of TM migration during the charging is similar in both compounds.

In the subsequent discharge process, we found that the anionic (O^{2-}/O^{n-} (n< 2)) redox occurs quite reversibly at ~~a~~ the high ~~redox~~ voltage region for O2-LLNMOs. As can be seen from mRIXS images in **Fig. 5b**, ~~for~~during the initial discharge ~~region ('3','4', and '5')~~, the oxidized oxygen feature dropped its intensity significantly from '3' to '4', and ~~gradually blurred as the cells discharged and~~ completely disappeared at '5' ~~state~~. ~~It~~ This indicates that majority of the ~~a continuous~~ oxygen reduction takes place at high potentials ('3' → ~~'5'~~'4') and is completed by '5'. ~~during discharge and t~~The ~~absence of~~ oxygen redox activity is thus completely absent at low potentials ('5' → '6'). Consistently, in STXM spectrum for the equivalent discharge region ('3' → '5'), ~~In the voltage range of the initial discharge ('3' → '4'),~~ the O K-edge peak at 531.~~5~~0 eV disappears, clearly indicating the reduction of O_{2p} states at high-voltage region. Moreover, the

18

signature of TM_{3d}–O_{2p} reduction was presented with the disappearance of the peak at 856 eV at the Ni L_3-edge as well as that at 529 eV at the O K-edge, indicating the simultaneous cationic (Ni^{4+} to Ni^{2+}) reduction. This observation is in contrast to the typical anionic redox behavior observed in the O3-LLNMOs, which was recently demonstrated with the major anionic redox activities at low potential region after the cation redox reaction.[33] And, this asymmetric anionic redox reaction for the charge (high potential charging) and the discharge (low potential discharging) was accounted for the voltage hysteresis of LLNMOs. In the O2-LLNMOs, on the other hand, the oxygen redox activity was solely observed at the high-voltage region without the signature in the low-voltage region ('45' → '56'), which is mainly compensated by partial manganese reduction (Supplementary Discussion 54). For O3-type LLNMCOs ($Li_{1.17}Ni_{0.21}Co_{0.08}Mn_{0.54}O_2$), Gent *et al*. demonstrated that the lowered discharge potential of anionic redox originates from the significant coordination loss of oxygen in the TM layer, whose originally coordinated TM ions move to the Li layer.[33] Such coordination loss of oxygen inevitably shifts the O_{2p} states to the higher level in the electronic structure, and thus decreases the voltage of oxygen redox. However, according to our STEM and theoretical observations, TM ions in the Li layer readily return to the TM layer upon re-lithiation of charged O2-LLNMOs, which would rapidly restore the coordination environment of oxygen. This behavior is dissimilar to that for O3-type compounds, wherein a substantial amount of TM ions remains in the Li layer. This finding implies that the anomalously symmetrical redox

properties of O2-LLNMOs must result from the facile return of migrated TM ions upon discharge. Mitigation of the asymmetry of the anionic redox may be beneficial to the long-term cyclability as it decreases the voltage hysteresis, although there have been few attempts aimed at improvement of the redox symmetry.

In order to further support the O redox at high potential discharge, several electrochemical tests were additionally performed. **Fig. 5**b presents two model dQ dV^{-1} experiments, in which the anionic redox is separated from TM–O redox by cycling two cells; (i) below 4.35 V without triggering of the O redox (black dotted line) and (ii) with O redox triggered (colored solid line). Excluding the cation redox activity (yellow region), the additional electrochemical activity achieved after the O redox triggered (blue region) is solely exhibited at the high potentials without any additional activities in the yellow region. The invariance of the cation redox region even after the O redox triggered is in line with the STXM data, supporting the anionic reduction at high redox potentials. In **Fig. 5**c, we also investigated the change in the discharge profiles of O2-LLNMOs as a function of the current density, considering that that anionic redox exhibits much more sluggish kinetics than cation redox, thus the variations of the anionic and cationic redox regimes are readily distinguishable.[32,46] Upon increasing the current density, the discharge capacity of the high-voltage region (above 3.4 V) steadily and drastically decreases from 136 mAh g^{-1} at 5 mA g^{-1} to 74 mAh g^{-1} at 200 mA g^{-1} (see **Fig. 5**d). However, the capacity of the redox region below 3.4 V is well

maintained with only minor changes of less than 6 mAh g^{-1} until the current density reaches 100 mA g^{-1}. The observation that the capacity fade at high rates mainly arises in the high-voltage region supports the sluggish anionic redox occurring in the high voltage range on discharge. Notably, it contrasts with that of O3-LLNMOs in which the substantial capacity drops are observed in both regions (above 3.4 V and below 3.4 V), which is attributed to anionic redox activity spread into the low-voltage region (Supplementary Fig. ~~14~~13).

Conclusion

In summary, we proposed a new strategy to improve the reversibility of TM migration by employing an O2-type structural framework wherein the cation migration path is effectively modified because of the unique site preferences. The intra-cycle reversible behavior of TM ions was visualized through STEM measurements, and complementary XRD, Raman spectroscopy, and HR-TEM analyses confirmed the preservation of the pristine structure over long-term cycling. Owing to this excellent reversibility, O2-LLNMOs exhibit remarkable reduction in voltage fade and redox asymmetry compared with their O3-phase counterparts. Theoretical calculations consistently presented that the intra-layer TM migration is thermodynamically prevented because of the large repulsion between face-sharing cations in O2-LLNMOs, facilitating the reverse migration. ~~This work provides robust guidance that will help steer strategies to resolve~~

the issues of voltage decay and hysteresis, with the implications that tailoring the site preference of TM ions may be an effective approach to modulate the reversibility of structural rearrangements during electrochemical cycling.

This work provides robust guidance that will help steer strategies to resolve the issues of voltage decay and hysteresis in a range of lithium-rich layered oxides. In a broader context, tailoring site preference to drive reversible cation migration is also applicable to other fields where irreversible cation migration is critical to performance degradation of materials, such as conventional layered cathodes[47,48], electrocatalysis[49], and photovoltaics.[50] Important directions for further study include exploring large chemical spaces within the O2 structural framework through the sensitive control of cation and anion composition. For example, recent studies have revealed for O3-LLNMOs and O3-LLNMCOs that migration tendencies of TM ions can be dependent on their metal composition.[7,23] Therefore, the combination of O2 structural framework and optimized lithium-rich chemistry will ensure the greatest structural reversibility and energy retention. Another remaining task for lithium-rich layered oxides is narrowing the gap between academic solutions and industrial needs with the improvement of engineering and synthetic process. Notably, alternative synthetic routes to produce O2 phase are needed to circumvent the cost and lithium loss issues associated with the ion-exchange method that was employed in this study.

Methods

Synthesis. To synthesize P2-Na$_{5/6}$(Li$_{0.2}$Ni$_{0.2}$Mn$_{0.6}$)O$_2$, stoichiometric amounts of LiCH$_3$COO•2H$_2$O (99%, Sigma-Aldrich), NaCH$_3$COO•3H$_2$O (99%, Sigma-Aldrich), Ni(CH$_3$COO)$_2$•4H$_2$O (98%, Sigma-Aldrich), and Mn(CH$_3$COO)$_2$•4H$_2$O (99%, Sigma-Aldrich) were dissolved in distilled water containing appropriate amounts of resorcinol (99%, Sigma-Aldrich) and formaldehyde. To mediate the volatility of lithium and sodium at high temperature, 5% excess of lithium and sodium sources were compensated by Li$_2$CO$_3$ (99.99%, Sigma-Aldrich) and Na$_2$CO$_3$ (99%, Sigma-Aldrich). The mixture was heated with continuous stirring at 70 °C for 2 h and then at 90 °C overnight without stirring. Finally, the P2 phase was obtained by additional heat treatment at 500 °C for 5 h and 900 °C for 10 h with intermediate grinding. In the following ion-exchange step, the resultant P2-phase powders were added to 10 times excess amount of 5 M LiBr (99%, Sigma-Aldrich) solution in hexanol and then heated at 120 °C for 24 h to obtain O2-phase material. After ion exchange, the product was rinsed with ethanol and distilled water several times. The entire ion-exchange process was repeated once more to complete the substitution of sodium with lithium.

Electrochemistry. The electrodes were fabricated using the following steps. A slurry of 80 wt% active materials, 10 wt% carbon black (Super P), and 10 wt% polyvinylidene fluoride dissolved in *N*-methyl-2-pyrrolidone

(NMP; 99.5%, Sigma-Aldrich) was cast onto aluminum foil. The resultant mixture was dried in a 70 °C vacuum oven overnight to allow the NMP to evaporate. Coin cells (CR2032, Hohsen) were assembled using the electrodes, a lithium counter electrode, a separator (GF/F filter, Whatman), and a 1 M solution of $LiPF_6$ in a mixture of ethyl carbonate and dimethyl carbonate (EC/DMC, 1:1 v/v) in an Ar-filled glove box. The galvanostatic charge/discharge process was performed in the voltage range of 2.0–4.8 V at room temperature using a potentio-galvanostat (WBCS 3000, WonA Tech).

XRD. as-prepared samples were characterized using XRD (D8 ADVANCE, Bruker, Bremen, Germany) with Cu-Kα radiation (λ=1.54178 Å) at a scanning speed of 0.167° min^{-1} in the 2θ range of 10°–70°. High-resolution powder diffraction (HRPD) was performed at beamline 9B at the Pohang Light Sources (PLS) in the Pohang Accelerator Laboratory (PAL), Republic of Korea. The data were collected over the 2θ range of 10°–133° with a step size of 0.01°, step time of 4 s, and wavelength of λ=1.5226 Å. Rietveld refinement of the XRD patterns was performed using the FullProf program.

Raman spectroscopy. Raman spectra of the pristine and 40-cycled electrodes were recorded using a Raman spectrometer (LabRAM HV Evolution, HORIBA, Japan) with an Ar laser as the excitation light source (λ=532 nm). The scattered light of the Raman signal was collected in a backscattering geometry using a 50× microscope objective lens. The data were measured using an acquisition time of 20 s and 10 accumulations.

The spectra were deconvoluted using the XPS Peak program.

XANES. XANES spectra of the harvested electrodes were obtained at beamline 7D at the PLS using a double-crystal monochromator containing two sets of Si(111) crystals. All the measurements were performed at room temperature, and the Ni and Mn K-edge spectra were collected in total electron yield mode. To accurately calibrate the energy scale and any drift of the monochromator position, metal foils were placed in a third chamber as a reference. All of the spectra were normalized and compared using the Athena program.

STXM. STXM analysis was performed at beamline 10A at the PLS to obtain the O K-edge and Ni and Mn L_3-edge spectra. Primary particles were drop-cast onto carbon-coated Cu TEM grids for the measurements. By keeping the focal position at the same particle, the two-dimensional transmitted photon intensity was recorded in pixel form at a fixed energy. To obtain image stacks, the same measurements were repeated over different X-ray energy ranges. The image stacks were acquired in 0.2 eV steps with a 2 ms dwell time and were aligned using the aXis 2000 software package.

SEM. Field-emission scanning electron microscopy (FE-SEM; SU-70, Hitachi, Japan) analysis was used to examine the surface morphological changes during the ion-exchange process. To compensate for the low conductivity of both materials, the active materials were coated with Pt nanoparticles three times.

HR-TEM. The electrodes harvested in the pristine state and after 40 cycles were sonicated into particles in ethanol and transferred onto carbon-coated Cu grids to obtain HR-TEM images and SAED patterns using field-emission transmission electron microscopy (FE-TEM; JEOL, JEM-2100F, Japan).

Cs-STEM. Cross-sectional TEM specimens of the as-prepared and cycled electrode slurry films were prepared using focused ion beam (FIB) milling (FEI, Helios 650). The prepared specimens were used for high-angle annular dark-field imaging under 80 keV using aberration-corrected STEM (Cs-STEM; JEOL, JEM-ARM200F, Japan) with a point-to-point resolution of 0.08 nm.

First-principles calculations. The first-principles calculations in this work were conducted based on spin-polarized DFT calculations, as implemented in the Vienna *ab initio* simulation package (VASP).[51] All the DFT energies were estimated within the GGA + U parameterization using the Perdew–Burke–Ernzerhof (PBE) functional.[52] Effective Hubbard-U parameters of 3.9 and 6.0 were applied to the 3d electrons of Mn and Ni atoms, respectively, in accordance with the values reported in previous works.[53,54] A plane-wave basis set was utilized with an energy cutoff of 520 eV and a 3 × 3 × 2 gamma-point-centered k-point mesh. ~~For all the cases~~ Unless otherwise stated, the lattice parameters and atomic positions were fully relaxed until the interatomic forces were smaller than 0.02 eV Å^{-1}. Detailed information regarding the model construction and TM migration analysis is provided in Supplementary Discussion 3.

mRIXS mRIXS experiments were performed in the iRIXS endstation at BL8.0.1 of the Advanced Light Source at Lawrence Berkeley National Laboratory.[55] The emission energy resolution is about 0.25 eV through a VLS-spectrograph. The excitation energy resolution is about 0.3 eV. Data were collected with 0.2 eV steps upon excitation energies across the whole Oxygen K absorption edge.

References

1	Larcher, D. & Tarascon, J. M. Towards greener and more sustainable batteries for electrical energy storage. *Nature Chemistry* **7**, 19 (2014).

2~~3~~	Li, W., Song, B. & Manthiram, A. High-voltage positive electrode materials for lithium-ion batteries. *Chemical Society Reviews* **46**, 3006-3059 (2017).

3~~5~~	Hong, J., Gwon, H., Jung, S.-K., Ku, K. & Kang, K. Review—Lithium-Excess Layered Cathodes for Lithium Rechargeable Batteries. *Journal of The Electrochemical Society* **162**, A2447-A2467 (2015).

4~~6~~	Assat, G. & Tarascon, J.-M. Fundamental understanding and practical challenges of anionic redox activity in Li-ion batteries. *Nature Energy* **3**, 373-386 (2018).

5~~8~~	Bettge, M. et al. Voltage Fade of Layered Oxides: Its Measurement and Impact on Energy Density. *Journal of The Electrochemical Society* **160**, A2046-A2055 (2013).

6~~9~~	Sathiya, M. et al. Origin of voltage decay in high-capacity layered oxide electrodes. *Nature Materials* **14**, 230 (2014).

7~~10~~	Ku, K. et al. Suppression of Voltage Decay through Manganese Deactivation and Nickel Redox Buffering in High-Energy Layered Lithium-Rich Electrodes. *Advanced Energy Materials* **8**, 1800606 (2018).

8~~11~~	Zheng, J. et al. Li- and Mn-Rich Cathode Materials: Challenges to Commercialization. *Advanced Energy Materials* **7**, 1601284 (2017).

9~~12~~	Mohanty, D. et al. Unraveling the Voltage-Fade Mechanism in High-Energy-Density Lithium-Ion Batteries: Origin of the Tetrahedral Cations for Spinel Conversion. *Chemistry of Materials* **26**, 6272-6280 (2014).

10~~13~~	Gallagher, K. G. et al. Correlating hysteresis and voltage fade in lithium- and manganese-rich layered transition-metal oxide

electrodes. *Electrochemistry Communications* **33**, 96-98 (2013).

11 ~~14~~ Kleiner, K. et al. Origin of High Capacity and Poor Cycling Stability of Li-Rich Layered Oxides: A Long-Duration in Situ Synchrotron Powder Diffraction Study. *Chemistry of Materials* **30**, 3656-3667 (2018).

12 ~~16~~ Gu, M. et al. Formation of the Spinel Phase in the Layered Composite Cathode Used in Li-Ion Batteries. *ACS Nano* **7**, 760-767 (2013).

13 ~~17~~ Hong, J. et al. Structural evolution of layered Li1.2Ni0.2Mn0.6O2 upon electrochemical cycling in a Li rechargeable battery. *Journal of Materials Chemistry* **20**, 10179-10186 (2010).

14 ~~18~~ Zheng, J. et al. Structural and Chemical Evolution of Li- and Mn-Rich Layered Cathode Material. *Chemistry of Materials* **27**, 1381-1390 (2015).

15 ~~20~~ Mohanty, D. et al. Correlating cation ordering and voltage fade in a lithium–manganese-rich lithium-ion battery cathode oxide: a joint magnetic susceptibility and TEM study. *Physical Chemistry Chemical Physics* **15**, 19496-19509 (2013).

16 ~~21~~ Wu, Y. et al. Probing the initiation of voltage decay in Li-rich layered cathode materials at the atomic scale. *Journal of Materials Chemistry A* **3**, 5385-5391 (2015).

17 ~~22~~ Rinaldo, S. G. et al. Physical Theory of Voltage Fade in Lithium- and Manganese-Rich Transition Metal Oxides. *Journal of The Electrochemical Society* **162**, A897-A904 (2015).

18 ~~23~~ Lee, E. & Persson, K. A. Structural and Chemical Evolution of the Layered Li-Excess LixMnO3 as a Function of Li Content from First-Principles Calculations. *Advanced Energy Materials* **4**, 1400498 (2014).

19 ~~24~~ Kim, S. et al. Material design of high-capacity Li-rich layered-oxide electrodes: Li2MnO3 and beyond. *Energy & Environmental Science* **10**, 2201-2211 (2017).

20 ~~25~~ Lim, J.-M. et al. The origins and mechanism of phase transformation in bulk Li2MnO3: first-principles calculations and experimental studies. *Journal of Materials Chemistry A* **3**, 7066-7076 (2015).

21 ~~26~~ Li, Q. et al. K+-Doped Li1.2Mn0.54Co0.13Ni0.13O2: A Novel Cathode Material with an Enhanced Cycling Stability for Lithium-Ion Batteries. *ACS Applied Materials & Interfaces* **6**, 10330-10341 (2014).

22 ~~27~~ Nayak, P. K., Grinblat, J., Levi, M. & Aurbach, D. Understanding the Effect of Lithium Bis(oxalato) Borate (LiBOB) on the Structural and Electrochemical Aging of Li and Mn Rich High Capacity Li1.2Ni0.16Mn0.56Co0.08O2 Cathodes. *Journal of The Electrochemical Society* **162**, A596-A602 (2015).

23 ~~28~~ Shi, J.-L. et al. Mitigating Voltage Decay of Li-Rich Cathode Material via Increasing Ni Content for Lithium-Ion Batteries. *ACS Applied Materials & Interfaces* **8**, 20138-20146 (2016).

24 ~~29~~ Reed, J. & Ceder, G. Role of Electronic Structure in the Susceptibility of Metastable Transition-Metal Oxide Structures to Transformation. *Chemical Reviews* **104**, 4513-4534 (2004).

25 ~~30~~ Du, K. et al. Exploring reversible oxidation of oxygen in a manganese oxide. *Energy & Environmental Science* **9**, 2575-2577

(2016).

26~~31~~ Rong, X. et al. Structure-Induced Reversible Anionic Redox Activity in Na Layered Oxide Cathode. *Joule* **2**, 125-140 (2018).

27~~33~~ Maitra, U. et al. Oxygen redox chemistry without excess alkali-metal ions in Na2/3[Mg0.28Mn0.72]O2. *Nature Chemistry* **10**, 288 (2018).

28~~34~~ Delmas, C., Braconnier, J.-J., Fouassier, C. & Hagenmuller, P. Electrochemical intercalation of sodium in NaxCoO2 bronzes. *Solid State Ionics* **3-4**, 165-169 (1981).

29~~35~~ Paulsen, J. M., Thomas, C. L. & Dahn, J. R. Layered Li-Mn-Oxide with the O2 Structure: A Cathode Material for Li-Ion Cells Which Does Not Convert to Spinel. *Journal of The Electrochemical Society* **146**, 3560-3565 (1999).

30~~36~~ Yabuuchi, N. et al. New O2/P2-type Li-Excess Layered Manganese Oxides as Promising Multi-Functional Electrode Materials for Rechargeable Li/Na Batteries. *Advanced Energy Materials* **4**, 1301453 (2014).

31~~37~~ de Boisse, B. M., Jang, J., Okubo, M. & Yamada, A. Cobalt-Free O2-Type Lithium-Rich Layered Oxides. *Journal of The Electrochemical Society* **165**, A3630-A3633 (2018).

32~~38~~ Assat, G. et al. Fundamental interplay between anionic/cationic redox governing the kinetics and thermodynamics of lithium-rich cathodes. *Nature Communications* **8**, 2219 (2017).

33~~39~~ Gent, W. E. et al. Coupling between oxygen redox and cation migration explains unusual electrochemistry in lithium-rich layered oxides. *Nature Communications* **8**, 2091 (2017).

34~~40~~ Hong, J. et al. Metal–oxygen decoordination stabilizes anion redox in Li-rich oxides. *Nature Materials* **18**, 256-265 (2019).

35~~41~~ Lim, J. et al. Origin and hysteresis of lithium compositional spatiodynamics within battery primary particles. *Science* **353**, 566 (2016).

36~~42~~ Li, X. et al. Direct Visualization of the Reversible O2−/O− Redox Process in Li-Rich Cathode Materials. *Advanced Materials* **30**, 1705197 (2018).

37~~43~~ Luo, K. et al. Anion Redox Chemistry in the Cobalt Free 3d Transition Metal Oxide Intercalation Electrode Li[Li0.2Ni0.2Mn0.6]O2. *Journal of the American Chemical Society* **138**, 11211-11218 (2016).

38~~44~~ Gao, S. et al. The Role of Various Components of Transition Metal Layer on the Properties of Li-Rich Cathode Li1.2[M0.4Mn0.4]O2 (M = Ni, Co, Ni1/2Mn1/2 and Fe). *Journal of The Electrochemical Society* **164**, A3824-A3831 (2017).

39~~45~~ Myeong, S. et al. Understanding voltage decay in lithium-excess layered cathode materials through oxygen-centred structural arrangement. *Nature Communications* **9**, 3285 (2018).

40~~46~~ Paulsen, J. M., Thomas, C. L. & Dahn, J. R. O2 Structure Li2/3[Ni1/3 Mn2/3]O2: A New Layered Cathode Material for Rechargeable Lithium Batteries. I. Electrochemical Properties. *Journal of The Electrochemical Society* **147**, 861-868 (2000).

41~~47~~ Konishi, H. et al. Potential hysteresis between charge and discharge

reactions in Li1.2Ni0.13Mn0.54Co0.13O2 for lithium ion batteries. *Solid State Ionics* **300**, 120-127 (2017).

4248 Konishi, H. et al. Origin of hysteresis between charge and discharge processes in lithium-rich layer-structured cathode material for lithium-ion battery. *Journal of Power Sources* **298**, 144-149 (2015).

4349 Hu, E. et al. Evolution of redox couples in Li- and Mn-rich cathode materials and mitigation of voltage fade by reducing oxygen release. *Nature Energy* **3**, 690-698 (2018).

44 Yang, W. & Devereaux, T. P. Anionic and cationic redox and interfaces in batteries: Advances from soft X-ray absorption spectroscopy to resonant inelastic scattering. *Journal of Power Sources* **389**, 188-197 (2018).

45 Wu, J. et al. Fingerprint Oxygen Redox Reactions in Batteries through High-Efficiency Mapping of Resonant Inelastic X-ray Scattering. *Condensed Matter* **4** (2019)Dai, K. et al. High reversibility of lattice oxygen redox quantified by direct bulk probes of both anionic and cationic redox reactions. *Joule 3, 518-541 (2019).*

4650 Assat, G., Iadecola, A., Delacourt, C., Dedryvère, R. & Tarascon, J.-M. Decoupling Cationic–Anionic Redox Processes in a Model Li-Rich Cathode via Operando X-ray Absorption Spectroscopy. *Chemistry of Materials* **29**, 9714-9724 (2017).

47 Manthiram, A., Knight, J. C., Myung, S.-T., Oh, S.-M. & Sun, Y.-K. Nickel-Rich and Lithium-Rich Layered Oxide Cathodes: Progress and Perspectives. *Advanced Energy Materials* **6**, 1501010 (2016).

48 Schipper, F. et al. Stabilizing nickel-rich layered cathode materials by a high-charge cation doping strategy: zirconium-doped LiNi0.6Co0.2Mn0.2O2. *Journal of Materials Chemistry A* **4**, 16073-16084 (2016).

49 Grimaud, A. et al. Activation of surface oxygen sites on an iridium-based model catalyst for the oxygen evolution reaction. *Nature Energy* **2**, 16189 (2016).

50 Domanski, K. et al. Migration of cations induces reversible performance losses over day/night cycling in perovskite solar cells. *Energy & Environmental Science* **10**, 604-613 (2017).

51 Kresse, G. & Furthmüller, J. Efficient iterative schemes for ab initio total-energy calculations using a plane-wave basis set. *Physical Review B* **54**, 11169-11186 (1996).

52 Dudarev, S. L., Botton, G. A., Savrasov, S. Y., Humphreys, C. J. & Sutton, A. P. Electron-energy-loss spectra and the structural stability of nickel oxide: An LSDA+U study. *Physical Review B* **57**, 1505-1509 (1998).

53 Seo, D.-H. et al. The structural and chemical origin of the oxygen redox activity in layered and cation-disordered Li-excess cathode materials. *Nature Chemistry* **8**, 692 (2016).

54 Jain, A. et al. A high-throughput infrastructure for density functional theory calculations. *Computational Materials Science* **50**, 2295-2310 (2011).

55 Qiao, R. et al. High-efficiency in situ resonant inelastic x-ray

scattering (iRIXS) endstation at the Advanced Light Source. *Review of Scientific Instruments* **88**, 033106 (2017).

Acknowledgements

Author contributions

D.E., B.K. and K.K. designed the project. D.E. carried out the synthesis, structural characterization, and electrochemical test and performed synchrotron-based measurements such as XRD, XANES, and STXM. B.K. conducted density functional theory calculations and analyzed the experimental results. S.J.K. performed HR-TEM measurement and interpreted all TEM data with simulations. H.P. and S.-P.C. conducted Raman spectroscopy and Cs-STEM analysis, respectively. G.Y. provided fundamental idea for density functional theory calculations. M.H.L. and O.T. acquired *ex situ* XRD and SEM data, respectively. S.-K.J. provided constructive advice for experimental design. J.W. and W.Y. measured and processed RIXS data. W.M.S., K.K., S.K.P., and I.H. offered valuable comments for this project. D.E., B.K., and K.K. wrote manuscript and K.K supervised all aspect of the research.

## Competing interests

The authors declare no competing interests.
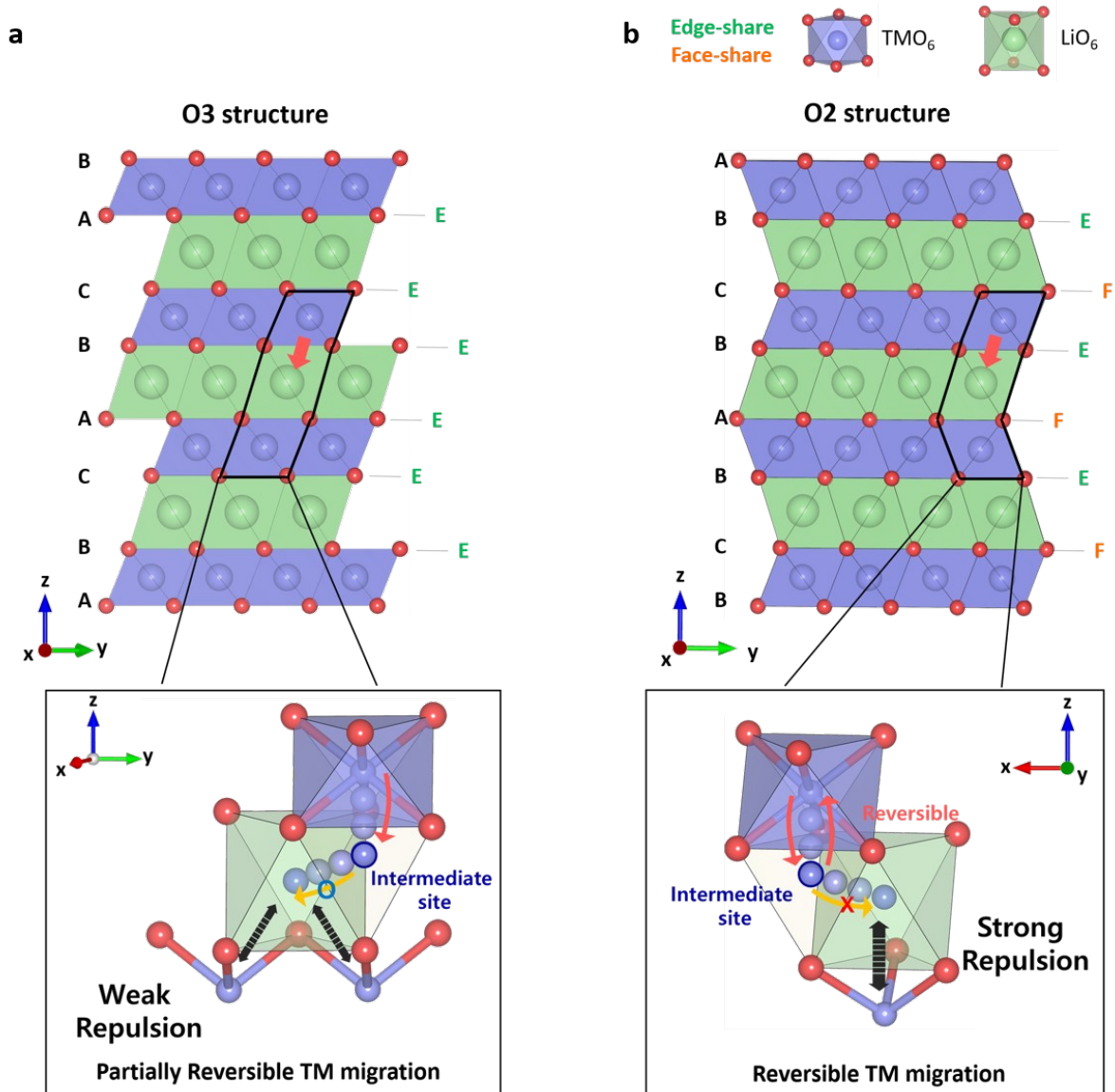
Fig. 1. Comparison of crystal structures and cation migration paths. Schematic illustrations of crystal structures of **a,** O3-type and **b,** O2-type lithium layered oxides. The figures below show the TM migration paths on a magnified scale. Although TM ions in the O3 structure can readily occupy Li sites that share only edges with neighboring cations, the TM ions in the O2 structure are subject to strong repulsion when they occupy Li sites face-sharing with neighboring cations.
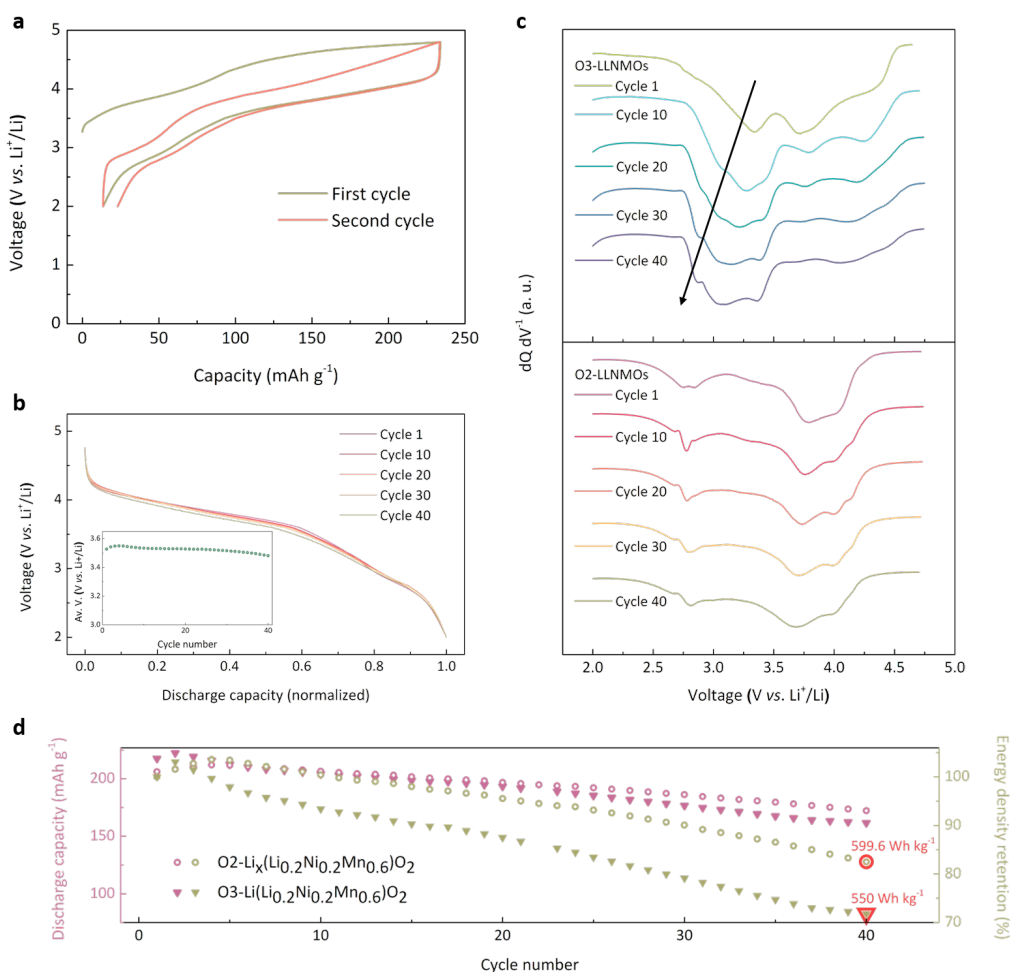
Fig. 2. Suppression of voltage decay in O2-LLNMOs. a, First and second charge–discharge curves of O2-LLNMOs cycled in the voltage range of 2.0–4.8 V at a current density of 5 mA g^{-1}. **b,** Normalized discharge curves of O2-LLNMOs for 40 cycles. The data were collected every 10 cycles. The inset shows the change in the average voltage over 40 cycles. **c,** Comparison of voltage decay in dQ dV^{-1} curves of O2- and O3-LLNMOs. The arrow in the profile of O3-LLNMOs highlights the drastic shift toward low voltage with cycling. **d,** Comparison of discharge capacity and energy density retention in O2- and O3-LLNMOs.

33
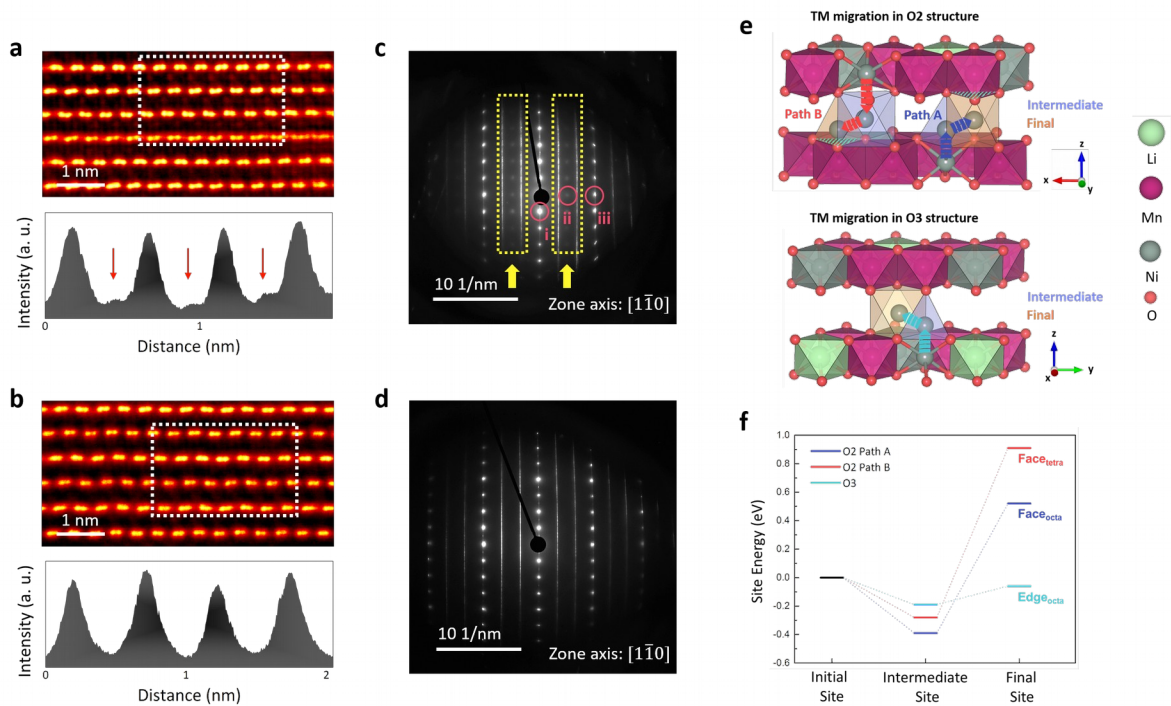
Fig. 3. Highly reversible cation migration in O2-LLNMOs. HAADF-STEM images along the $[1\bar{1}0]$ zone axis for **a,** 4.8-V charged and **b,** 2.0-V discharged O2-LLNMOs. The graphs below are the HAADF signal profiles of the regions enclosed by the dotted lines in the STEM images. The arrows in the signal profile of the charged sample indicate the evolution of TM_{Li} defects. SAED patterns of **c,** 4.8-V charged and **d,** 2.0-V discharged O2-LLNMOs along the $[1\bar{1}0]$ direction. The extra spots in the areas enclosed by the yellow dotted boxes in **c** represent significant cation migration into the Li layers. In **c**, spots marked with red circles correspond to (i) $00\bar{2}$ (ordered structure and cation-disordered structure), (ii) 110 (cation-disordered structure), and (iii) the overlap of 110 (ordered structure) and 220 (cation-disordered structure), respectively. Other spots are indexed in Supplementary Fig. 7. **e,** TM migration paths from initial to intermediate and final Li sites. **f,** Relative site energies of intermediate and final sites calculated along the migration path of TM ions.
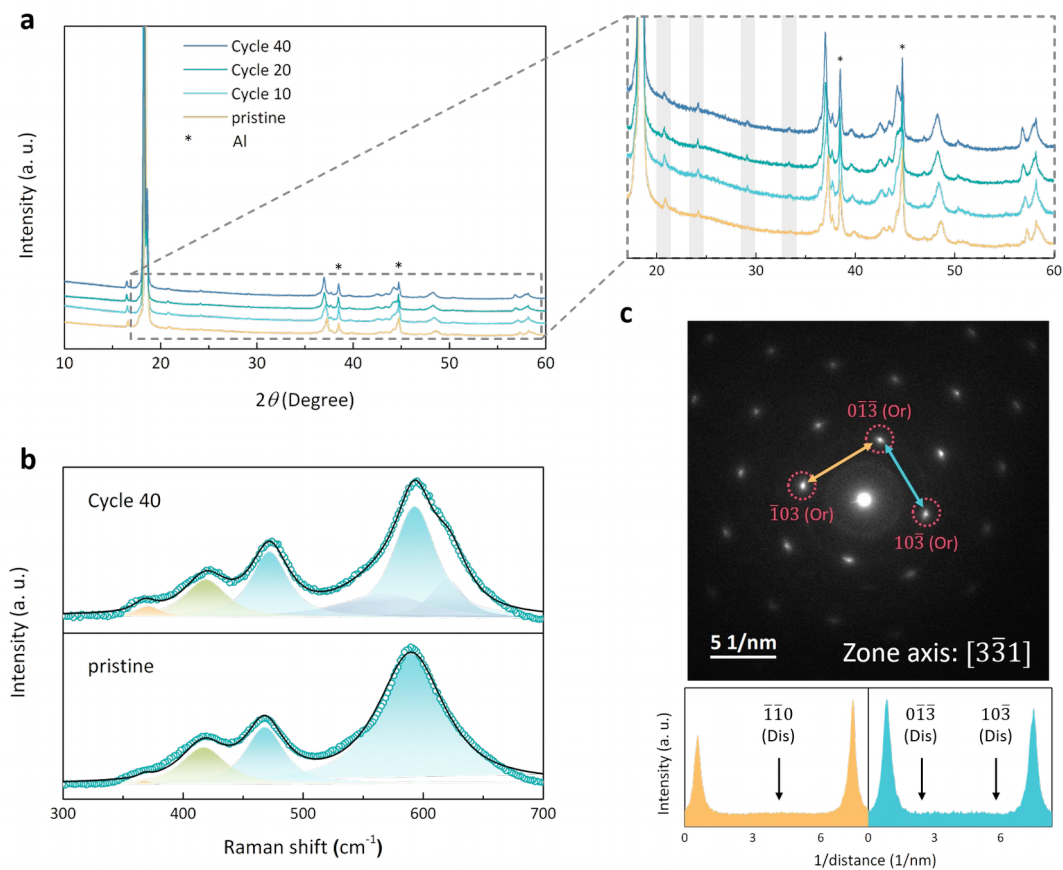
Fig. 4. Mitigation of structural evolution in O2-LLNMOs for 40 cycles. a, *Ex situ* XRD patterns of pristine and 10-, 20-, and 40-cycled O2-LLNMOs. The magnified view clearly shows honeycomb superstructure peaks (grey shaded). A magnified view of the region between 19° and 35° is presented in the inset. **b,** Comparison of Raman spectra for pristine and 40-cycled samples. The newly emerging blue peaks at 627 and 572 cm^{-1} after 40 cycles correspond to the layered-to-spinel transitions. **c,** SAED pattern of O2-LLNMOs along the $[3\bar{3}1]$ zone axis after 40 cycles (top, Or: ordered). SAED signal profiles for yellow and blue lines in SAED pattern (bottom, Dis: disordered). The arrows indicate the

expected positions of additional spots of disordered O2-LLNMOs.
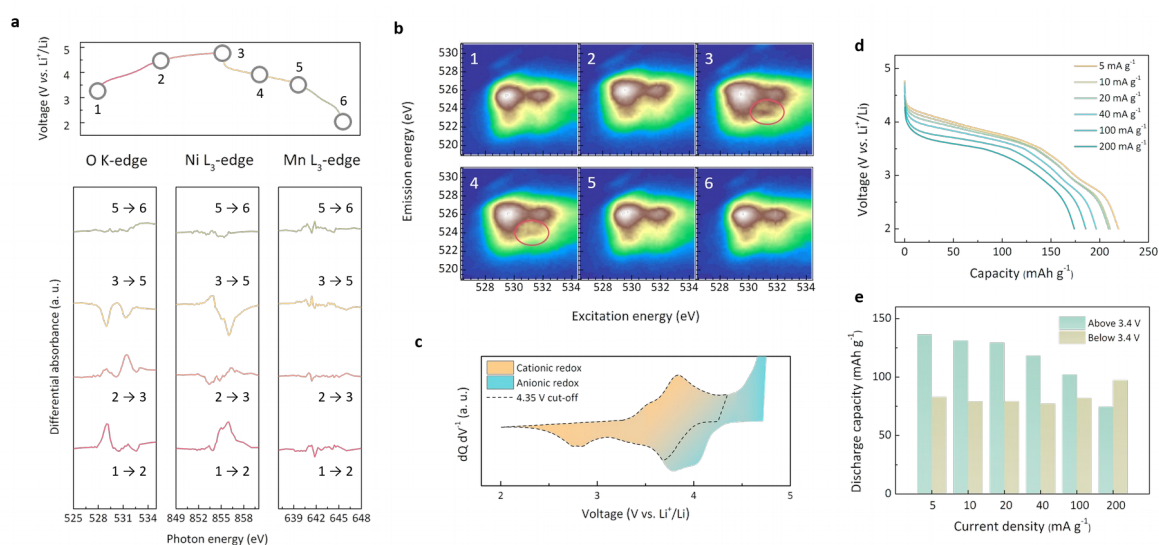
Figure 5. Anomalous anionic redox behavior in O2-LLNMOs. a, STXM differential absorbance spectra of O K-edge and Ni, Mn L_3-edges for the first charge and discharge cycle. Each spectrum shows the difference between two ~~adjacent~~ designated points in the electrochemical curve. **b,** O K-edge mRIXS of O2-LLNMOs for the first cycle obtained at each point of **a**. Distinct oxygen redox features are indicated by red circles. ~~b,~~**c,** dQ dV^{-1} curve of O2-LLNMOs measured at a current density of 5 mA g^{-1}. ~~c,~~**d,** Electrochemical curves of O2-LLNMOs for current densities ranging from 5 to 200 mA g−1. ~~d,~~**e,** Variation of discharge capacity as a function of current density estimated for the two classified voltage ranges, 2.0–3.4 V and 3.4–4.8 V.